



Primitive to conventional geometry projection for efficient phonon transport calculations

Xun Li, Simon Thébaud, Lucas Lindsay

► To cite this version:

Xun Li, Simon Thébaud, Lucas Lindsay. Primitive to conventional geometry projection for efficient phonon transport calculations. npj Computational Materials, 2023, 9 (1), pp.193. 10.1038/s41524-023-01148-8 . hal-04265039

HAL Id: hal-04265039

<https://hal.science/hal-04265039>

Submitted on 30 Oct 2023

HAL is a multi-disciplinary open access archive for the deposit and dissemination of scientific research documents, whether they are published or not. The documents may come from teaching and research institutions in France or abroad, or from public or private research centers.

L'archive ouverte pluridisciplinaire **HAL**, est destinée au dépôt et à la diffusion de documents scientifiques de niveau recherche, publiés ou non, émanant des établissements d'enseignement et de recherche français ou étrangers, des laboratoires publics ou privés.

ARTICLE OPEN



Primitive to conventional geometry projection for efficient phonon transport calculations

Xun Li¹, Simon Thébaud² and Lucas Lindsay¹✉

The primitive Wigner-Seitz cell and corresponding first Brillouin zone (FBZ) are typically used in calculations of lattice vibrational and transport properties as they contain the smallest number of degrees of freedom and thus have the cheapest computational cost. However, in complex materials, the FBZ can take on irregular shapes where lattice symmetries are not apparent. Thus, conventional cells (with more atoms and regular shapes) are often used to describe materials, though dynamical and transport calculations are more expensive. Here we discuss an efficient anharmonic lattice dynamic method that maps conventional cell dynamics to primitive cell dynamics based on translational symmetries. Such symmetries have not been utilized in typical lattice dynamical calculations. This leads to phase interference conditions that act like conserved quantum numbers and a conservation rule for phonon scattering that is hidden in conventional dynamics which significantly reduces the computational cost. We demonstrate this method for phonon transport in a variety of materials with inputs from first-principles calculations and attribute its efficiency to reduced scattering phase space and fewer summations in scattering matrix element calculations.

npj Computational Materials (2023)9:193; <https://doi.org/10.1038/s41524-023-01148-8>

INTRODUCTION

Computational studies of material properties, particularly transport phenomena of heat, charge, and mass at micro- and nanoscales¹, have recently provided accurate quantification of measured observables and fundamental understanding of complex physics, due in large part to increased computational power, theoretical advances, and availability of numerical tools^{2–6}. First-principles calculations based on density functional theory (DFT) have demonstrated remarkable power in accurately predicting thermal and electrical properties of semiconductors^{7–10}, for example, the ultrahigh thermal conductivity of cubic BAs and BN^{11–14}, phonon hydrodynamics in graphitic materials^{15–17}, and high mobility of BAs¹⁸. Many of these successful simulations have been based on materials with simple structures and compositions. More recently, researchers have been exploring more complex materials with correspondingly diverse and novel properties including large thermal resistance^{19,20}, anomalous thermal Hall effect^{21–23}, and topological superconductivity^{24–26}, though this requires more extensive computational power due to much larger degrees of freedom.

Calculations and simulations of crystalline material properties are typically based on periodically arranged unit cells that contain the smallest number of degrees of freedom, i.e., the primitive unit cell. The most widely used primitive cells, for which basic properties can be described, are called Wigner-Seitz cells²⁷ (WSC; real space) and their corresponding first Brillouin zones (FBZ; reciprocal space). These are typically used for calculations of lattice vibrational and transport properties because they have the cheapest computational cost. However, such calculations, particularly in complex crystals, often have awkward geometries with WSC and FBZ having irregular, non-intuitive shapes in Cartesian space. For example, bismuth telluride (Bi₂Te₃, space group R-3m) has a primitive cell with an angle of 24° between pairs of lattice vectors. This adds difficulty in analyzing properties along natural high-symmetry lines (in-plane and cross-plane) as these require

projection from the oblique lattice vectors. On the other hand, there are alternative unit cells with different geometries that can fill space and respect natural symmetries. Experiments, in particular, tend to probe and analyze material properties from these more convenient conventional geometries where the symmetries of the lattice are obvious and straightforward. For example, the inelastic neutron scattering measurement studied the structural phase transition in a GeTe conventional cell²⁸. This makes the comparison between primitive cell calculations and conventional cell measurements more challenging. One solution is to perform calculations based on conventional unit cells, however, the number of vibrational degrees of freedom of the conventional unit cell can be 2–3 times larger than those of the primitive unit cell, thus giving a much larger computational burden²⁹. For example, the hexagonal conventional cell of Bi₂Te₃ has 15 atoms with 45 vibrational modes, which is three times larger compared to that of the primitive unit cell. As a result, calculations of material properties based on conventional geometries, especially quasiparticle dynamics and transport phenomena (to be discussed in this work), are more expensive because of the increased cost in calculating interactions. In particular, lowest order three-phonon scattering processes scale to the cubic power of the number of degrees of freedom, thus phonon transport calculations for the conventional cell of Bi₂Te₃ will cost around 27 times more than those of the primitive unit cell.

It is well known that the choice of unit cell is arbitrary and should underly the same physical behaviors; however, it is not well known how to use symmetry relations to make lattice dynamical calculations more efficient in larger unit cells. Taking advantage of both the convenience of conventional geometries and lower degrees of freedom of primitive geometries, we previously proposed and demonstrated an efficient dynamic method for calculating quasiparticle dispersions, phonons in particular³⁰. There, we discussed that mapping of conventional cell dynamics to primitive cell dynamics using internal translational symmetries

¹Materials Science and Technology Division, Oak Ridge National Laboratory, Oak Ridge, TN, USA. ²Univ Rennes, INSA Rennes, CNRS, Institut FOTON-UMR 6082, Rennes, France. ✉email: lindsaylr@ornl.gov

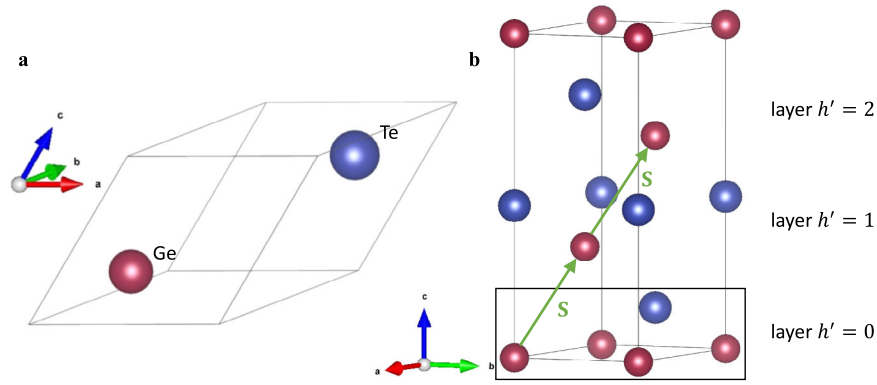


Fig. 1 Crystal structure of GeTe (R3m space group). **a** Two-atom primitive unit cell where each pair of lattice vectors forms an angle of 57.8°. **b** Six-atom conventional unit cell with three layers related by translation vector \mathbf{S} (green arrows). The black rectangle highlights that a single layer can be used to describe the dynamics in a conventional unit cell.

saves computational cost in dynamical matrix diagonalizations and leads to phase interference conditions demonstrated through comparison of calculated phonon dispersions with measured inelastic neutron scattering spectra.

In this work, we apply this primitive to conventional cell dynamic method based on primitive translational symmetry (PTS) to thermal transport calculations limited by anharmonic interactions. In conventional geometries, this PTS dynamic method significantly reduces the computational cost of thermal conductivity calculations by reducing the quasiparticle scattering phase space through a conservation rule that is hidden in typical conventional dynamics and reducing the number of summations in scattering matrix element calculations. We demonstrate the convenience of this PTS method by calculating phonon transport properties based on DFT for three materials from different space groups: GeTe with space group R3m, solid N_2 with space group $\text{I}2_13$, and ferromagnetic CrCl_3 with space group R-3. These are representative materials with different levels of complexity in conventional cells and have important applications in thermoelectrics (GeTe)^{31–34}, energy storage (N_2)^{35,36}, and two-dimensional magnetism (CrCl_3)^{37–41}.

RESULTS

PTS dynamics in conventional basis

Figure 1 depicts the primitive (a) and conventional (b) geometries for GeTe with space group R3m. In this figure, the translation vector \mathbf{S} relates the primitive and conventional geometries and is fractional within the conventional cell. In general, \mathbf{S} is $(n_x\mathbf{R}_1 + n_y\mathbf{R}_2 + n_z\mathbf{R}_3)/N$ where \mathbf{R}_1 , \mathbf{R}_2 , and \mathbf{R}_3 are conventional lattice basis vectors, N is the number of layers in the conventional unit cell, and n_x , n_y , and n_z are integers related to a particular material's space group (discussed below). This fractional translational symmetry can be used to reorganize the dynamical matrix of the conventional unit cell and more explicitly demonstrate the vibrational phases between layers.³⁰

$$D_{\alpha\beta}^{kk'}(\mathbf{q}, l) = \frac{1}{\sqrt{m_k m_{k'}}} \sum_{h'p'} \Phi_{\alpha\beta}^{00k, h'p'k'} e^{i\mathbf{q} \cdot \mathbf{R}_{p'}} e^{ih'(\mathbf{q} \cdot \mathbf{S} + 2\pi l/N)} \quad (1)$$

where Greek subscripts are Cartesian directions, k loops over the atoms in a single layer of the conventional unit cell, \mathbf{q} is a phonon wavevector, m_k is the mass of atom k , $\mathbf{R}_{p'}$ is a lattice vector locating the p' conventional cell (integer multiples of the basis vectors above), N is the number of 'primitive' layers within the conventional cell, h' represents each of these layers ranging from 0 to $N-1$ (see labels in Fig. 1 for GeTe), $\Phi_{\alpha\beta}^{00k, h'p'k'}$ are harmonic interatomic force constants (IFCs) between atom k in the origin layer and atom k' in the p' conventional cell in layer h' , and $e^{ih'2\pi l/N}$ is the vibrational phase between layers. Derivation of Eq. 1 is

provided in Supplementary Note 1. In this formalism, l is an integer representing the phase degree of freedom between the layers that also ranges from 0 to $N-1$. It acts as a conserved quantity in scattering processes (via phase interference conditions) within the conventional unit cell (discussed below) that limits the scattering phase space³⁰. Equation 1 represents $N \times 3n \times 3n$ dynamical matrices for each \mathbf{q} , which gives the same number of phonon branches as those from the single conventional $3Nn \times 3Nn$ dynamical matrix, where n is the number of atoms in one layer of the conventional cell. Diagonalization of Eq. 1 for $N \times 3n \times 3n$ matrices is computationally more efficient than diagonalizing a single $3Nn \times 3Nn$ matrix. Note that the primitive cell dynamics consists of a single $3n \times 3n$ dynamical matrix.

Specifically, for GeTe (space group: R3m) with conventional unit cell shown in Fig. 1b, there are three layers with two atoms in each ($N = 3$ and $n = 2$). The translation vector $\mathbf{S} = (2\mathbf{R}_1 + \mathbf{R}_2 + \mathbf{R}_3)/3 = [a/2, a/(2\sqrt{3}), c/3]$ where a and c are in-plane and out-of-plane lattice parameters, respectively. Instead of one conventional 18×18 dynamical matrix, Eq. (1) with PTS dynamics gives three 6×6 dynamical matrices for $l = (0, 1, 2)$ for each \mathbf{q} .

The PTS dynamics of Eq. 1 can be applied to 81 different space groups with symmetry operations $x + n_x/N$, $y + n_y/N$, $z + n_z/N$, where N is either 2 or 3, and n_α ranges from 0 to 2 with $n_x n_y n_z \neq 0$. Table 1 summarizes the allowed space groups corresponding to such operations. We demonstrate the application of PTS dynamics on representative materials: GeTe with space group R3m, solid N_2 with space group $\text{I}2_13$, and ferromagnetic CrCl_3 with space group R-3. We note that the solid N_2 system considered here has not been synthesized, presumably due to predicted thermodynamic instability⁴², but provides a good test case of our method due to N_2 having the $\text{I}2_13$ space group and a relatively simple structure. Complete results for GeTe and temperature dependent thermal conductivities for all materials are presented in the main text. Structures, phonon dispersions, and scattering rates for CrCl_3 and solid N_2 are described in a previous study³⁰ and in Supplementary Figs. 2–4, respectively. Details of DFT calculations for all materials are provided in Methods.

Phonon dispersion

We first examine the vibrational properties of GeTe based on its conventional unit cell (Fig. 1b). Diagonalizing Eq. (1) for each value of $l = (0, 1, 2)$ gives the phonon dispersion depicted in Fig. 2 with six branches for each vibrational phase depicted by different colors. The phonon dispersions from the PTS dynamics overlap those from the conventional method (underlying black solid curves) as observed along high-symmetry lines and an arbitrary direction in reciprocal space. The colored dispersions provide insights into observables from scattering experiments in

Table 1. Space groups for which PTS dynamics can be applied to conventional unit cells.

Symmetry operations	Space groups
$[x, y + 1/2, z + 1/2], [x + 1/2, y + 1/2, z], [x + 1/2, y, z + 1/2]$	C2, Cm, Cc, C2/m, C2/c, C222 ₁ , C222, Cmm2, Cmc2 ₁ , Ccc2, Cmc _m , Cmca, Cmmm, Cccm, Cmme, Ccce, F222, Fmm2, Fdd2, Fmmm, Fddd, F23, Fm-3, Fd-3, F432, F4 ₃ 2, F-43m, F-43c, Fm-3m, Fm-3c, Fd-3m, Fd-3c, Amm2, Aem2, Ama2, Aea2
$[x + 1/2, y + 1/2, z + 1/2]$	I222, I2 ₁ 2 ₁ 2 ₁ , Imm2, Iba2, Ima2, Immm, Ibam, Ibca, Imma, I4, I4 ₁ , I-4, I4/m, I4 ₁ /a, I422, I4 ₁ 22, I4mm, I4cm, I4 ₁ md, I4 ₁ cd, I-4m2, I-4c2, I-42m, I-42d, I4/mmm, I4/mcm, I4 ₁ /amd, I4 ₁ /acd, I23, I2 ₁ 3, Im-3, Ia-3, I432, I4 ₁ 32, I-43m, I-43d, Im-3m, Ia-3d
$[x + 2/3, y + 1/3, z + 1/3], [x + 1/3, y + 2/3, z + 2/3]$	R3, R-3, R32, R3m, R3c, R-3m, R-3c

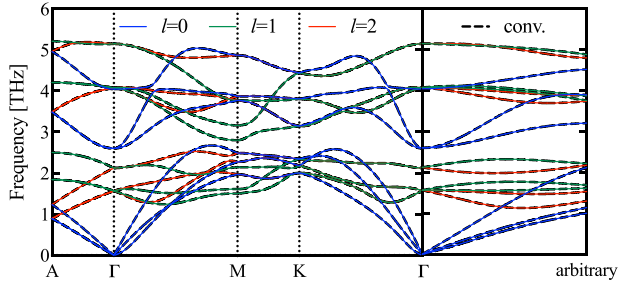


Fig. 2 Primitive and conventional phonon dispersions of GeTe. Underlying dashed black curves give the phonon dispersions of GeTe from conventional dynamics, while the colored solid curves give these from PTS dynamics, both along high-symmetry lines and an arbitrary direction from the Γ point to ($q_x = 0.123\pi/a$, $q_y = 0.456\pi/b$, $q_z = 0.789\pi/c$). Blue, green, and red curves correspond to integers $l = 0$, $l = 1$, and $l = 2$, respectively.

conventional geometries as only phonon branches with $l = 0$ give non-zero spectral intensities, which has been demonstrated for CrCl_3 ³⁰ and other materials with internal twist symmetries^{43,44}.

The wavevector \mathbf{q} and integer l are not limited to the FBZ and can be calculated for extended Brillouin zones. When comparing phonons from different zones, for instance mapping extended zones back to the FBZ, which is necessary for studying Umklapp phonon scattering, $\Delta\mathbf{q}$ relating phonons between zones is given by a reciprocal lattice vector: $\Delta\mathbf{q} = \mathbf{G} = [g_1\mathbf{G}_1, g_2\mathbf{G}_2, g_3\mathbf{G}_3]$, an integer (g_i) multiple of the conventional reciprocal lattice basis vectors (\mathbf{G}_i)²⁹. In this mapping, \mathbf{q} and l are related through a conserved phase relation obtained from Eq. (1): $\Delta\mathbf{q} \cdot \mathbf{S} + 2\pi\Delta l/N = 0$ (see Methods for a detailed derivation), where the change of integer l is given by $\Delta l = l_G = -(n_x g_1 + n_y g_2 + n_z g_3)$. Again, n_a are given by the space group of the crystal (see Table 1). This relationship was demonstrated for bulk CrCl_3 when comparing calculated dispersions to scattering measurements in varying Brillouin zones³⁰ and is shown for GeTe in Supplementary Fig. 1 (see Methods for details).

Scattering conservation rule from phase relations

The PTS dynamic method also elucidates conservation conditions for intrinsic phonon-phonon interactions enforced by phase relations represented by the integer l that are hidden in the conventional dynamics used to build phonon linewidths³⁰. This scattering is critically important when trying to determine and understand thermal transport in conventional geometries.

To demonstrate this, we start with anharmonic three-phonon transition rates from quantum perturbation theory (i.e., Fermi's

golden rule)^{45–47}

$$\Gamma_{\lambda\lambda'\lambda''}^{\pm} = \frac{\hbar\pi}{4N_{\text{uc}}} \frac{(f_{\lambda}^0 + 1)(f_{\lambda'}^0 + 1/2 \pm 1/2)f_{\lambda''}^0}{\omega_{\lambda}\omega_{\lambda'}\omega_{\lambda''}} |V_{\lambda, \pm\lambda', -\lambda''}^{(3)}|^2 \delta(\omega_{\lambda} \pm \omega_{\lambda'} - \omega_{\lambda''}) \quad (2)$$

where λ represents a phonon mode with wavevector \mathbf{q} and polarization J , the Dirac delta function δ ensures energy conservation, N_{uc} is the number of conventional unit cells, primes label different phonon modes, $V_{\lambda, \pm\lambda', -\lambda''}^{(3)}$ are three-phonon scattering matrix elements, and f_{λ}^0 is the Bose-Einstein distribution for mode λ . The \pm designate two different types of three-phonon interactions, coalescence and decay⁴⁸. The scattering matrix elements in conventional dynamics are

$$V_{\lambda, \pm\lambda', -\lambda''}^{(3)} = \sum_K \sum_{p'K'} \sum_{p''K''} \sum_{a\beta\gamma} \Phi_{a\beta\gamma}^{0K, p'K', p''K''} e^{i\mathbf{q}' \cdot \mathbf{R}_{p'}} e^{i\mathbf{q}'' \cdot \mathbf{R}_{p''}} \frac{\xi_{aK}^{\lambda} \xi_{\beta K'}^{\lambda'} \xi_{\gamma K''}^{\lambda''}}{\sqrt{m_K m_{K'} m_{K''}}} \quad (3)$$

where K refers to atoms in the conventional cell, ξ_{aK}^{λ} is the a component of an eigenvector in the conventional basis for phonon mode λ , and $\Phi_{a\beta\gamma}^{0K, p'K', p''K''}$ are third-order anharmonic IFCs⁴⁷. Translational invariance has already been enforced in Eq. (3), which leads to crystal momentum conservation for three-phonon interactions:⁴⁹

$$\mathbf{q} \pm \mathbf{q}' - (\mathbf{q}'' + \mathbf{G}) = 0 \quad (4)$$

that limits the scattering phase space.

We now discuss an additional conservation rule of the integer l in the PTS dynamic method. An eigenvector in the conventional basis is related to that in PTS dynamics through³⁰

$$\xi_{aK}^{\lambda} = \frac{1}{\sqrt{N}} \tilde{\xi}_{aK}^{\lambda} e^{i\mathbf{h}(\mathbf{q} \cdot \mathbf{S} + 2\pi l/N)} \quad (5)$$

Where $\tilde{\xi}_{aK}^{\lambda}$ is the a component of the PTS eigenvector for atom k in a single layer. λ represents a phonon mode with wavevector \mathbf{q} , phase integer l , and polarization j (as determined by diagonalization of Eq. 1). Combining Eqs. (3) and (5) and replacing atom notation (K) with (h, k) and phonon state notation λ (\mathbf{q}, J) with $\tilde{\lambda}$ (\mathbf{q}, j, l), as with Eq. 1, we have

$$\begin{aligned} V_{\tilde{\lambda}, \pm\tilde{\lambda}', -\tilde{\lambda}''}^{(3)} &= \left(\frac{1}{\sqrt{N}}\right)^3 \sum_{h0k} \sum_{h'p'k'} \sum_{h''p''k''} \\ &\times \sum_{a\beta\gamma} \Phi_{a\beta\gamma}^{h0k, h'p'k', h''p''k''} e^{\pm i\mathbf{q}' \cdot \mathbf{R}_{p'}} e^{-i\mathbf{q}'' \cdot \mathbf{R}_{p''}} \\ &\times \frac{\tilde{\xi}_{aK}^{\tilde{\lambda}} \tilde{\xi}_{\beta K'}^{\tilde{\lambda}'} \tilde{\xi}_{\gamma K''}^{\tilde{\lambda}''}}{\sqrt{m_K m_{K'} m_{K''}}} e^{i\mathbf{h}(\mathbf{q} \cdot \mathbf{S} + 2\pi l/N)} e^{\pm i\mathbf{h}'(\mathbf{q}' \cdot \mathbf{S} + 2\pi l'/N)} e^{-i\mathbf{h}''(\mathbf{q}'' \cdot \mathbf{S} + 2\pi l''/N)} \end{aligned} \quad (6)$$

The interatomic potential (to all perturbative orders) is invariant with respect to translation by a lattice vector (in both primitive and conventional bases), thus anharmonic IFCs are invariant with respect to integer multiples of the layer translation vector \mathbf{S} so

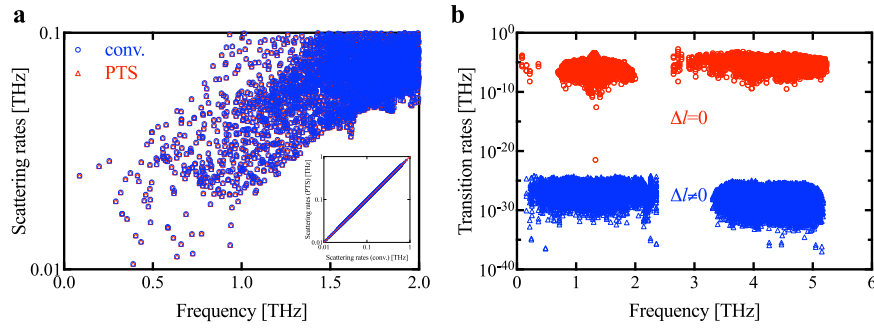


Fig. 3 Total scattering and individual transition rates for phonons in GeTe. a Scattering rates as a function of phonon frequency from separate conventional (blue) and PTS (red) dynamics. Inset: Direct comparison of scattering rates from the two methods. An underlying solid red line provides a guide for the eye showing equality. **b** Individual anharmonic phonon transition rates for a phonon mode at the Γ point with ($\omega = 2.61$ THz, $j = 4$) as a function of the frequency of one of the other interacting modes in three-phonon interactions. Transition rates with $\Delta l \neq 0$, i.e., violating conservation of l , are numerically zero.

that

$$\Phi_{\alpha\beta\gamma}^{h0k,h'p'k',h''p''k''} = \Phi_{\alpha\beta\gamma}^{00k,(h'-h)p'k',(h''-h)p''k''} \quad (7)$$

Note that the unit cell p' (p'') will be shifted if $h' < h$ ($h'' < h$). The layer phase relations in Eq. (6) are also unchanged if shifted by h :

$$e^{ih(\mathbf{q}\cdot\mathbf{S}+2\pi l/N)} e^{\pm ih'(\mathbf{q}'\cdot\mathbf{S}+2\pi l'/N)} e^{-ih''(\mathbf{q}''\cdot\mathbf{S}+2\pi l''/N)} \\ = e^{\pm i(h'-h)(\mathbf{q}'\cdot\mathbf{S}+2\pi l'/N)} e^{-i(h''-h)(\mathbf{q}''\cdot\mathbf{S}+2\pi l''/N)} \quad (8)$$

Rearranging Eq. 8 and using Eq. 4 lead to the following constraint

$$e^{ih\mathbf{S}\cdot\mathbf{G}} e^{i2\pi h(l \pm l' - l'')/N} = 1 \quad (9)$$

Thus,

$$h[-l_G + (l \pm l' - l'')] = 0 \quad (10)$$

where $l_G = -N\mathbf{S}\cdot\mathbf{G}/(2\pi)$ is an integer (see Methods for further discussion of the relationship of \mathbf{G} and l_G). Since h can be any integer, the expression in the bracket must be zero

$$l \pm l' - (l'' + l_G) = 0 \quad (11)$$

Equation (11) reveals another conservation rule in terms of integer l that is hidden in conventional methods. Explicitly using this conservation condition reduces the scattering phase space by $\sim 1/N$ and enables significantly more efficient transport calculations (described below). We note that the primitive and conventional cell calculations have the additional phase symmetry constraint (Eq. 11) built in, however, the primitive cell has awkward geometries and the conventional cell does not explicitly exploit it, simply giving no strength to scattering interactions that violate Eq. 11.

Scattering and thermal transport

We now continue to show how scattering matrix elements $V_{\tilde{\lambda}, \pm \tilde{\lambda}', -\tilde{\lambda}}^{(3)}$ are calculated to obtain scattering rates (Eq. (2)) in PTS dynamics. Applying translational invariance to the third-order potential expansion (and relabeling the arbitrary layer indices in Eqs. 7 and 8), the scattering matrix elements in PTS dynamics become

$$V_{\tilde{\lambda}, \pm \tilde{\lambda}', -\tilde{\lambda}}^{(3)} = \left(\frac{1}{\sqrt{N}}\right)^3 \sum_{h0k} \sum_{h'p'k'} \sum_{h''p''k''} \\ \times \sum_{\alpha\beta\gamma} \Phi_{\alpha\beta\gamma}^{00k,h'p'k',h''p''k''} e^{i\mathbf{q}'\cdot\mathbf{R}_{p'}} e^{i\mathbf{q}''\cdot\mathbf{R}_{p''}} \\ \times \frac{\epsilon_{\alpha k}^{\tilde{\lambda}} \epsilon_{\beta k'}^{\pm \tilde{\lambda}'} \epsilon_{\gamma k''}^{\mp \tilde{\lambda}''}}{\sqrt{m_k m_{k'} m_{k''}}} e^{\pm ih'(\mathbf{q}'\cdot\mathbf{S}+2\pi l'/N)} e^{-ih''(\mathbf{q}''\cdot\mathbf{S}+2\pi l''/N)} \quad (12)$$

Since the terms in the summation are independent of h , the summation over h gives a factor N and Eq. (12) becomes

$$V_{\tilde{\lambda}, \pm \tilde{\lambda}', -\tilde{\lambda}}^{(3)} = \frac{1}{\sqrt{N}} \sum_{00k} \sum_{h'p'k'} \sum_{h''p''k''} \\ \times \sum_{\alpha\beta\gamma} \Phi_{\alpha\beta\gamma}^{00k,h'p'k',h''p''k''} e^{i\mathbf{q}'\cdot\mathbf{R}_{p'}} e^{i\mathbf{q}''\cdot\mathbf{R}_{p''}} \\ \times \frac{\epsilon_{\alpha k}^{\tilde{\lambda}} \epsilon_{\beta k'}^{\pm \tilde{\lambda}'} \epsilon_{\gamma k''}^{\mp \tilde{\lambda}''}}{\sqrt{m_k m_{k'} m_{k''}}} e^{\pm ih'(\mathbf{q}'\cdot\mathbf{S}+2\pi l'/N)} e^{-ih''(\mathbf{q}''\cdot\mathbf{S}+2\pi l''/N)} \quad (13)$$

We show in Fig. 3a that the scattering rates of GeTe from PTS dynamics are identical (within numerical accuracy) to those from conventional dynamics. Figure 3b shows the transition rates⁴⁹ for a representative phonon mode at the Γ point with ($\omega = 2.61$ THz, $j = 4$) as a function of the frequency of one of the interacting phonons ($\omega_{\lambda'}$) calculated from conventional dynamics. Here, PTS dynamics was used to identify the integer l for each of the three phonon modes involved in the interactions to determine whether conservation of l occurred or not: $\Delta l = l \pm l' - (l'' + l_G) = 0$ or $\Delta l \neq 0$. In Fig. 3b, the transition rates for $\Delta l \neq 0$ are numerically zero compared to those for $\Delta l = 0$. This demonstrates that conservation of l , which is mandated by the internal translational symmetry, is hidden in the conventional formalism suggesting that this can be used to reduce computational cost in thermal transport calculations.

The thermal conductivity matrix from the PTS dynamic method is calculated as

$$\kappa = \sum_{\tilde{\lambda}} C_{\tilde{\lambda}} v_{\tilde{\lambda}}^2 \tau_{\tilde{\lambda}} \quad (14)$$

where $C_{\tilde{\lambda}}$ is the volumetric specific heat for phonon mode $\tilde{\lambda}$ with wavevector \mathbf{q} , polarization j , and phase integer l , \mathbf{v} is the phonon velocity vector, and $\tau_{\tilde{\lambda}}$ is the phonon lifetime due to intrinsic three-phonon scattering (related to the inverse of the sum of scattering rates that conserve energy, momentum, and l) and isotopic scattering (in natural samples). Note that phonon branch J in the conventional basis is broken down into j and l in PTS dynamics. This is the only difference from the widely used formula in the conventional method^{7,47,49–51}. The PTS dynamic method gives identical thermal conductivities as the conventional method for both in-plane and cross-plane directions. Importantly, unlike phonon chirality previously described by a twist dynamical method^{43,44}, here PTS is not limited to specific high-symmetry directions, and thus calculations that involve sums over the full Brillouin zone (i.e., including low-symmetry points in reciprocal space), are possible. This is an important feature for application of the PTS dynamics to transport phenomena of quasiparticles.

Figure 4 shows the thermal conductivities of bulk N_2 , GeTe, and CrCl_3 as a function of temperature from 30 to 400 K. The crystalline N_2 system considered here (a non-molecular solid that exists

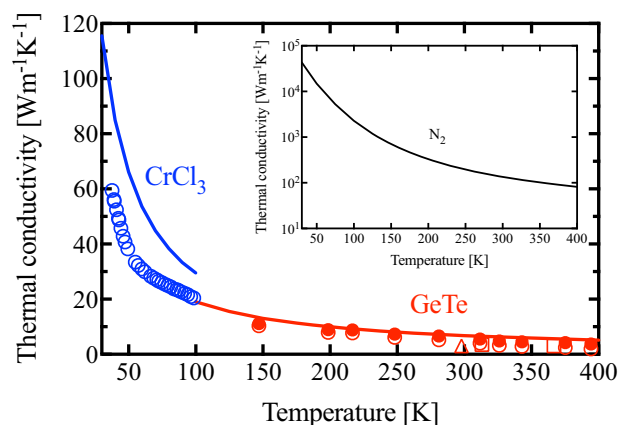


Fig. 4 Thermal conductivity of N_2 (black curve, inset), GeTe (blue curve), and $CrCl_3$ (red curve) from PTS dynamics as a function of temperature in bulk naturally occurring samples. Measurements for GeTe are represented by solid and open red circles⁵⁴, squares⁵⁵, and triangle⁵⁶. In-plane thermal conductivity measurements for $CrCl_3$ are represented by blue circles⁵⁷.

under high pressure^{35,36} has isotropic thermal transport, i.e., $\kappa_{xx} = \kappa_{yy} = \kappa_{zz}$ (off-diagonal terms are zero for all systems considered here), and has the highest κ of the three systems considered, with room temperature $\kappa = 150.35 \text{ Wm}^{-1}\text{K}^{-1}$. We note that N_2 has a reasonably high thermal conductivity, particularly at low temperature, due to its being comprised of covalently bonded light atoms in a relatively simple structure⁵², though it is significantly less thermally conductive than diamond⁵³. We also note that naturally occurring N is nearly isotopically pure, thus phonon-isotope scattering does not provide significant thermal resistance in the temperature range considered here.

GeTe and $CrCl_3$ have anisotropic thermal conductivity tensors with separate in-plane ($\kappa_{xx} = \kappa_{yy}$) and cross-plane (κ_{zz}) values; furthermore, phonon-isotope scattering is relatively important in each (see Supplementary Fig. 5). In Fig. 4 we compare in-plane κ for $CrCl_3$ and an effective thermal conductivity ($\kappa_{\text{eff}} = (2\kappa_{xx} + \kappa_{zz})/3$) for GeTe with measured values^{54–57}. Natural isotopes are included in the calculations for both cases. For GeTe, the crystal orientation of the thin film samples was not given (thus κ_{eff} was used here for comparison) and significant electronic contributions to κ are anticipated from measured resistance data. Thus, we compare our phonon calculations with both the total measured κ (filled red circles) for GeTe thin films and the expected lattice contribution (hollow red circles, subtracting estimated electronic κ via the Wiedemann-Franz law)⁵⁴. For ferromagnetic $CrCl_3$, spin-phonon interactions are expected to be important (not considered in this work), particularly at low temperatures. Here, we compare with measurements under the strongest applied in-plane magnetic field, which suppresses scattering by magnetic excitations so that nearly only intrinsic phonon scattering dominates the transport, particularly in the temperature range considered here⁵⁷. Agreement with measurements is reasonable given that phonon-defect interactions (i.e., from point defects, grain boundaries, surfaces, and other extended point defects) have not been considered. This suggests that the samples are relatively crystalline and pure.

Computational efficiency

To demonstrate the improved efficiency of PTS dynamics over the conventional dynamics, we calculate the ratio of total cpu hours required for PTS and conventional thermal conductivity calculations for GeTe, N_2 , and $CrCl_3$ (having different degrees of complexity) for different integration grid densities. The

computational savings is generally independent of the density of the sampling q mesh (Supplementary Fig. 6), and the average (over different grid densities) computational cost ratios are 0.3942 ± 0.0151 for N_2 ($N=2$, $n=4$), 0.1334 ± 0.0051 for GeTe ($N=3$, $n=2$), and 0.0925 ± 0.0054 for $CrCl_3$ ($N=3$, $n=8$). These results demonstrate that using PTS in the calculation of thermal transport in the conventional basis can give $\sim N^2$ numerical savings, particularly when the complexity of the material increases (as in going from N_2 to GeTe to $CrCl_3$). We also tested a very large toy system developed from GeTe and observed a similar speedup (see Supplementary Note 2 and Supplementary Fig. 7 for details). Overall, PTS dynamics in the conventional basis is significantly more efficient than conventional dynamics, which is especially beneficial for calculations of large complex conventional cells.

The efficiency of the PTS dynamic method for calculating phonon transport in a conventional basis comes in two-fold: reduced dynamical matrix sizes for harmonic calculations and reduced phase space and matrix sums for anharmonic calculations. In our particular transport framework³, the reciprocal space is discretized and phonon harmonic properties are calculated once for a given q mesh. Thus, the numerical savings for dynamical matrix diagonalizations are negligible compared with the much heavier anharmonic calculations. We find that the reduction of $\sim 1/N^2$ in computational cost for GeTe and $CrCl_3$ is primarily derived from two factors in anharmonic calculations. First, the conservation of integer l in Eq. (11) leads to reduced phase space that is $\sim 1/N$ compared to that in conventional dynamics. Moreover, the first summation in Eq. (13) is only for atoms in a single layer rather than all atoms in the conventional cell, which contributes to another $1/N$ factor in the calculation of scattering rates, which is the primary numerical cost in thermal conductivity calculations.

DISCUSSION

It is worth mentioning that our calculation framework, i.e., precalculated harmonic phonon properties on a fixed q mesh, is the same as that in widely used packages like ShengBTE³, almaBTE⁴, ALAMODE⁵, and phono3py⁶. Thus, the proposed PTS dynamic method can achieve a similar computational savings of $\sim 1/N^2$ with appropriate modifications in these applications.

Also, this PTS dynamics can be particularly efficient when applied to higher-order anharmonic scattering, for example, four-phonon scattering^{58,59}. In such cases, the scattering rates and scattering matrix elements are $\Gamma_{\lambda\lambda'\lambda''\lambda'''}^{\pm}$ and $V_{\lambda,\pm\lambda',\pm\lambda'',-\lambda'''}^{(4)}$, respectively, where λ''' represents a fourth phonon mode⁵⁸. Replacing the conventional description with PTS dynamics and following the same derivation, the conservation of integer l in Eq. (11) becomes $l \pm l' \pm l'' - (l''' + l_G) = 0$ where l''' corresponds to λ''' . A similar reduction of $\sim 1/N^2$ in computational cost is expected, which is especially beneficial considering that the four-phonon scattering rate calculations are thousands of times more expensive than those of three-phonon calculations⁵⁸.

In summary, we discussed lattice dynamics and phonon transport using an efficient dynamic method that uses primitive translational symmetry (PTS) within conventional cells. Such symmetry relations do not introduce new physical behaviors but can significantly simplify calculations in large complex unit cells. The underlying phase dynamics of quasiparticle interactions elucidate quantum phase interference conditions hidden in anharmonic phonon interactions within conventional unit cells, leading to conservation rules that can be exploited to make more efficient calculations of quasiparticle dynamics in larger, more convenient conventional unit cells, comparable to those of more awkward primitive unit cells. The proposed dynamics accurately describes transport phenomena and costs significantly less computationally compared to conventional dynamics, which

is valuable for studying quasiparticle interactions in complex material systems.

METHODS

Density functional theory

We performed density functional theory calculations using the projector augmented wave method (PAW)⁶⁰, as implemented in the Vienna Ab-initio Simulation Package (VASP)^{61–63}, for all the materials considered. The generalized gradient approximation, parameterized by Perdew, Burke, and Ernzerhof⁶⁴ was used for exchange-correlations.

The plane wave energy cut-off is 500 eV (520 eV for CrCl₃), and energy convergence criteria is 10⁻⁶ eV. Ionic relaxations were performed until Hellmann-Feynman forces converged to 10⁻⁵ eV/Å for GeTe and solid N₂ (10⁻⁴ eV/Å for CrCl₃). The structures were optimized with Γ -centered 9 × 9 × 3 (GeTe), 9 × 9 × 9 (solid N₂), and 4 × 4 × 4 (CrCl₃) *k*-meshes. Harmonic IFCs were calculated using the phonopy package⁶⁵ with a 4 × 4 × 2 supercell and Γ -centered 3 × 3 × 1 *k*-mesh for GeTe, a 3 × 3 × 3 supercell and Γ -centered 3 × 3 × 3 *k*-mesh for solid N₂, and a 2 × 2 × 1 supercell and Γ -centered 2 × 2 × 2 *k*-mesh for CrCl₃.

The anharmonic IFCs were calculated by finite displacement method using the thirdorder.py package³. For GeTe, a 300-atom 5 × 5 × 2 supercell, Γ -only *k*-mesh, and a cutoff distance up to the 5th nearest neighbors (NN) were used. For solid N₂, a 216-atom 3 × 3 × 3 supercell, Γ -centered 3 × 3 × 3 *k*-mesh, and a cutoff distance up to the 3rd NN were used. For CrCl₃, the interlayer spacing is much larger than the in-plane nearest neighbor atomic distances, thus we used a cylindrical cutoff that is 0.43 nm in the plane and 0.6 nm across the plane. The cutoffs correspond to the 7th NN in the plane and include most of the atoms in adjacent layers across the plane. A 192-atom 2 × 2 × 2 supercell and Γ -only *k*-mesh were used. All the other calculation parameters are the same as those used for harmonic calculations.

Zone folding relation between *q* and *l*

Translational invariance of the harmonic interatomic potential with respect to PTS requires that

$$e^{i\mathbf{q} \cdot (\mathbf{R}_p + \mathbf{h}'\mathbf{S})} e^{\frac{i\mathbf{h}'\mathbf{2}\pi}{N}} = e^{i\mathbf{q} \cdot (\mathbf{R}_p + (\mathbf{h}' - \mathbf{h})\mathbf{S})} e^{i\mathbf{h}(\mathbf{h}' - \mathbf{h})\mathbf{2}\pi/N} \\ = e^{i\mathbf{q} \cdot (\mathbf{R}_p + \mathbf{h}'\mathbf{S})} e^{i\mathbf{q} \cdot (-\mathbf{h}\mathbf{S})} e^{\frac{i\mathbf{h}'\mathbf{2}\pi}{N}} e^{-\frac{i\mathbf{h}\mathbf{2}\pi}{N}} \quad (15)$$

Rearranging Eq. (15) and comparing terms leads to

$$e^{i\mathbf{q}\mathbf{S}} e^{\frac{i\mathbf{2}\pi}{N}} = 1 \quad (16)$$

and thus

$$\mathbf{q} \cdot \mathbf{S} + \frac{2\pi}{N} l = 0 \quad (17)$$

where the translation vector \mathbf{S} is $[\frac{n_x}{N}\mathbf{R}_1, \frac{n_y}{N}\mathbf{R}_2, \frac{n_z}{N}\mathbf{R}_3]$. For extended zones, where \mathbf{q} is changed by $\Delta\mathbf{q} = \mathbf{G} = [g_1\frac{2\pi}{\mathbf{R}_1}, g_2\frac{2\pi}{\mathbf{R}_2}, g_3\frac{2\pi}{\mathbf{R}_3}]$, the change of integer *l* is thus

$$\Delta l = l_G = -\frac{N}{2\pi} \mathbf{G} \cdot \mathbf{S} = -(n_x g_1 + n_y g_2 + n_z g_3) \quad (18)$$

This relationship is shown via the phonon dispersion across two BZs for GeTe in Supplementary Fig. 1.

Thermal conductivity calculations

The numerical cost of the thermal conductivity calculations was computed for a variety of reciprocal space integration mesh densities for each system (Supplementary Fig. 6). For the data presented in Fig. 4 the *q*-mesh samplings used are 29 × 29 × 29 (N₂), 25 × 25 × 10 (GeTe), and 15 × 15 × 5 (CrCl₃), for which thermal conductivities are converged.

For both conventional and PTS dynamic methods, thermal conductivities are calculated by solving the steady-state Peierls-Boltzmann equation under the relaxation time approximation. The Dirac delta functions for energy conservation in Eq. (2) are approximated by adaptive Gaussian functions as implemented in the ShengBTE package³.

DATA AVAILABILITY

The data that support the findings of this study are available from the corresponding author upon reasonable request.

CODE AVAILABILITY

The custom codes for PTS dynamic method are available from the corresponding author on reasonable request.

Received: 13 February 2023; Accepted: 4 October 2023;

Published online: 16 October 2023

REFERENCES

- Chen, G. *Nanoscale energy transport and conversion: a parallel treatment of electrons, molecules, phonons, and photons*. (Oxford University Press, 2005).
- Madsen, G. K. & Singh, D. J. BoltzTraP. A code for calculating band-structure dependent quantities. *Comput. Phys. Commun.* **175**, 67–71 (2006).
- Li, W., Carrete, J., Katcho, N. A. & Mingo, N. ShengBTE: a solver of the Boltzmann transport equation for phonons. *Comput. Phys. Commun.* **185**, 1747–1758 (2014).
- Carrete, J. et al. almaBTE: A solver of the space-time dependent Boltzmann transport equation for phonons in structured materials. *Comput. Phys. Commun.* **220**, 351–362 (2017).
- Tadano, T., Gohda, Y. & Tsuneyuki, S. Anharmonic force constants extracted from first-principles molecular dynamics: applications to heat transfer simulations. *J. Condens. Matter Phys.* **26**, 225402 (2014).
- Togo, A., Chaput, L. & Tanaka, I. Distributions of phonon lifetimes in Brillouin zones. *Phys. Rev. B* **91**, 094306 (2015).
- Lindsay, L., Hua, C., Ruan, X. & Lee, S. Survey of ab initio phonon thermal transport. *Mater. Today Phys.* **7**, 106–120 (2018).
- McGaughey, A. J., Jain, A., Kim, H.-Y. & Fu, B. Phonon properties and thermal conductivity from first principles, lattice dynamics, and the Boltzmann transport equation. *J. Appl. Phys.* **125**, 011101 (2019).
- Ono, T., Fujimoto, Y. & Tsukamoto, S. First-principles calculation methods for obtaining scattering waves to investigate transport properties of nanostructures. *Quantum Matter* **1**, 4–19 (2012).
- Giustino, F. Electron-phonon interactions from first principles. *Rev. Mod. Phys.* **89**, 015003 (2017).
- Lindsay, L., Broido, D. & Reinecke, T. First-principles determination of ultrahigh thermal conductivity of boron arsenide: a competitor for diamond? *Phys. Rev. Lett.* **111**, 025901 (2013).
- Kang, J. S., Li, M., Wu, H., Nguyen, H. & Hu, Y. Experimental observation of high thermal conductivity in boron arsenide. *Science* **361**, 575–578 (2018).
- Li, S. et al. High thermal conductivity in cubic boron arsenide crystals. *Science* **361**, 579–581 (2018).
- Tian, F. et al. Unusual high thermal conductivity in boron arsenide bulk crystals. *Science* **361**, 582–585 (2018).
- Huberman, S. et al. Observation of second sound in graphite at temperatures above 100 K. *Science* **364**, 375–379 (2019).
- Machida, Y., Matsumoto, N., Isono, T. & Behnia, K. Phonon hydrodynamics and ultrahigh-room-temperature thermal conductivity in thin graphite. *Science* **367**, 309–312 (2020).
- Jeong, J., Li, X., Lee, S., Shi, L. & Wang, Y. Transient hydrodynamic lattice cooling by picosecond laser irradiation of graphite. *Phys. Rev. Lett.* **127**, 085901 (2021).
- Shin, J. et al. High ambipolar mobility in cubic boron arsenide. *Science* **377**, 437–440 (2022).
- Li, W. & Mingo, N. Ultralow lattice thermal conductivity of the fully filled skutterudite YbFe₄Sb₁₂ due to the flat avoided-crossing filler modes. *Phys. Rev. B* **91**, 144304 (2015).
- Yang, J., Jain, A. & Ong, W.-L. Inter-channel conversion between population-/coherence-channel dictates thermal transport in MAPbI₃ crystals. *Mater. Today Phys.* **28**, 100892 (2022).
- Ideue, T., Kurumaji, T., Ishiwata, S. & Tokura, Y. Giant thermal Hall effect in multiferroics. *Nat. Mater.* **16**, 797–802 (2017).

22. Yokoi, T. et al. Half-integer quantized anomalous thermal Hall effect in the Kitaev material candidate α -RuCl₃. *Science* **373**, 568–572 (2021).
23. Zhou, X. et al. Anomalous thermal Hall effect and anomalous Nernst effect of CsV₃Sb₅. *Phys. Rev. B* **105**, 205104 (2022).
24. Kezilebieke, S. et al. Topological superconductivity in a van der Waals heterostructure. *Nature* **588**, 424–428 (2020).
25. Nayak, A. K. et al. Evidence of topological boundary modes with topological nodal-point superconductivity. *Nat. Phys.* **17**, 1413–1419 (2021).
26. Masuko, M. et al. Nonreciprocal charge transport in topological superconductor candidate Bi₂Te₃/PdTe₂ heterostructure. *npj Quantum Mater.* **7**, 104 (2022).
27. Wigner, E. & Seitz, F. On the constitution of metallic sodium. *Phys. Rev.* **43**, 804 (1933).
28. Chattopadhyay, T. & Boucherle, J. Neutron diffraction study on the structural phase transition in GeTe. *J. Phys. C: Solid State Phys.* **20**, 1431 (1987).
29. Ashcroft, N. W. & Mermin, N. D. *Solid state physics*. (Cengage Learning, 1976).
30. Li, X. et al. Phonons and phase symmetries in bulk CrCl₃ from scattering measurements and theory. *Acta Mater.* **241**, 118390 (2022).
31. Jiang, B. et al. High figure-of-merit and power generation in high-entropy GeTe-based thermoelectrics. *Science* **377**, 208–213 (2022).
32. Hong, M., Zou, J. & Chen, Z. G. Thermoelectric GeTe with diverse degrees of freedom having secured superhigh performance. *Adv. Mater.* **31**, 1807071 (2019).
33. Li, J. et al. Low-symmetry rhombohedral GeTe thermoelectrics. *Joule* **2**, 976–987 (2018).
34. Zhang, X. et al. GeTe thermoelectrics. *Joule* **4**, 986–1003 (2020).
35. Yao, Y. & Adeniyi, A. O. Solid nitrogen and nitrogen-rich compounds as high-energy-density materials. *Phys. Status Solidi B* **258**, 2000588 (2021).
36. Eremets, M. I., Hemley, R. J., Mao, H.-K. & Gregoryanz, E. Semiconducting non-molecular nitrogen up to 240 GPa and its low-pressure stability. *Nature* **411**, 170–174 (2001).
37. Duong, D. L., Yun, S. J. & Lee, Y. H. van der Waals layered materials: opportunities and challenges. *ACS Nano* **11**, 11803–11830 (2017).
38. McGuire, M. A. Crystal and magnetic structures in layered, transition metal dihalides and trihalides. *Crystals* **7**, 121 (2017).
39. McGuire, M. A. Cleavable magnetic materials from van der Waals layered transition metal halides and chalcogenides. *J. Appl. Phys.* **128**, 110901 (2020).
40. Burch, K. S., Mandrus, D. & Park, J.-G. Magnetism in two-dimensional van der Waals materials. *Nature* **563**, 47–52 (2018).
41. Li, H., Ruan, S. & Zeng, Y. J. Intrinsic van der Waals magnetic materials from bulk to the 2D limit: new frontiers of spintronics. *Adv. Mater.* **31**, 1900065 (2019).
42. Jain, A. et al. Commentary: The Materials Project: A materials genome approach to accelerating materials innovation. *APL Mater.* **1**, 011002 (2013).
43. Juneja, R. et al. Phonons in complex twisted crystals: Angular momenta, interactions, and topology. *Phys. Rev. B* **106**, 094310 (2022).
44. Juneja, R. et al. Quasiparticle twist dynamics in non-symorphic materials. *Mater. Today Phys.* **21**, 100548 (2021).
45. Fermi, E. *Nuclear physics: a course given by Enrico Fermi at the University of Chicago*. (University of Chicago Press, 1950).
46. Omini, M. & Sparavigna, A. Beyond the isotropic-model approximation in the theory of thermal conductivity. *Phys. Rev. B* **53**, 9064 (1996).
47. Broido, D., Ward, A. & Mingo, N. Lattice thermal conductivity of silicon from empirical interatomic potentials. *Phys. Rev. B* **72**, 014308 (2005).
48. Ziman, J. M. *Electrons and phonons: the theory of transport phenomena in solids*. (Oxford university press, 2001).
49. Broido, D. A., Malorny, M., Birner, G., Mingo, N. & Stewart, D. A. Intrinsic lattice thermal conductivity of semiconductors from first principles. *Appl. Phys. Lett.* **91**, 231922 (2007).
50. Lindsay, L. First principles peierls-boltzmann phonon thermal transport: a topical review. *Nanoscale Microscale Thermophys. Eng.* **20**, 67–84 (2016).
51. Lindsay, L., Katre, A., Cepellotti, A. & Mingo, N. Perspective on ab initio phonon thermal transport. *J. Appl. Phys.* **126**, 050902 (2019).
52. Slack, G. A. Nonmetallic crystals with high thermal conductivity. *J. Phys. Chem. Solids* **34**, 321–335 (1973).
53. Wei, L., Kuo, P., Thomas, R., Anthony, T. & Banholzer, W. Thermal conductivity of isotopically modified single crystal diamond. *Phys. Rev. Lett.* **70**, 3764 (1993).
54. Nath, P. & Chopra, K. Thermal conductivity of amorphous and crystalline Ge and GeTe films. *Phys. Rev. B* **10**, 3412 (1974).
55. Ghosh, K., Kusiak, A., Noé, P., Cyrille, M.-C. & Battaglia, J.-L. Thermal conductivity of amorphous and crystalline GeTe thin film at high temperature: experimental and theoretical study. *Phys. Rev. B* **101**, 214305 (2020).
56. Fallica, R. et al. Effect of nitrogen doping on the thermal conductivity of GeTe thin films. *Phys. Status Solidi RRL* **7**, 1107–1111 (2013).
57. Pocs, C. A. et al. Giant thermal magnetoconductivity in CrCl₃ and a general model for spin-phonon scattering. *Phys. Rev. Res.* **2**, 013059 (2020).
58. Feng, T., Lindsay, L. & Ruan, X. Four-phonon scattering significantly reduces intrinsic thermal conductivity of solids. *Phys. Rev. B* **96**, 161201 (2017).
59. Han, Z., Yang, X., Li, W., Feng, T. & Ruan, X. FourPhonon: An extension module to ShengBTE for computing four-phonon scattering rates and thermal conductivity. *Comput. Phys. Commun.* **270**, 108179 (2022).
60. Blöchl, P. E. Projector augmented-wave method. *Phys. Rev. B* **50**, 17953 (1994).
61. Kresse, G. & Furthmüller, J. Efficiency of ab-initio total energy calculations for metals and semiconductors using a plane-wave basis set. *Comput. Mater. Sci.* **6**, 15–50 (1996).
62. Kresse, G. & Furthmüller, J. Efficient iterative schemes for ab initio total-energy calculations using a plane-wave basis set. *Phys. Rev. B* **54**, 11169 (1996).
63. Kresse, G. & Joubert, D. From ultrasoft pseudopotentials to the projector augmented-wave method. *Phys. Rev. B* **59**, 1758 (1999).
64. Perdew, J. P., Burke, K. & Ernzerhof, M. Generalized gradient approximation made simple. *Phys. Rev. Lett.* **77**, 3865 (1996).
65. Togo, A. & Tanaka, I. First principles phonon calculations in materials science. *Scr. Mater.* **108**, 1–5 (2015).

ACKNOWLEDGEMENTS

This work was supported by the U.S. Department of Energy, Office of Science, Basic Energy Sciences, Materials Sciences and Engineering Division. The calculations used resources of the Compute and Data Environment for Science (CADES) at the Oak Ridge National Laboratory, supported by the Office of Science of the U.S. Department of Energy under Contract No. DE-AC05-00OR22725, and resources of the National Energy Research Scientific Computing Center, supported by the Office of Science of the U.S. Department of Energy under Contract No. DE-AC02-05CH11231.

AUTHOR CONTRIBUTIONS

L.L. and S.T. conceived the idea. L.L. supervised the work. X.L. performed the calculations and wrote the manuscript with inputs from S.T. and L.L. All authors commented and revised the manuscript.

COMPETING INTERESTS

The authors declare no competing interests.

ADDITIONAL INFORMATION

Supplementary information The online version contains supplementary material available at <https://doi.org/10.1038/s41524-023-01148-8>.

Correspondence and requests for materials should be addressed to Lucas Lindsay.

Reprints and permission information is available at <http://www.nature.com/reprints>

Publisher's note Springer Nature remains neutral with regard to jurisdictional claims in published maps and institutional affiliations.



Open Access This article is licensed under a Creative Commons Attribution 4.0 International License, which permits use, sharing, adaptation, distribution and reproduction in any medium or format, as long as you give appropriate credit to the original author(s) and the source, provide a link to the Creative Commons license, and indicate if changes were made. The images or other third party material in this article are included in the article's Creative Commons license, unless indicated otherwise in a credit line to the material. If material is not included in the article's Creative Commons license and your intended use is not permitted by statutory regulation or exceeds the permitted use, you will need to obtain permission directly from the copyright holder. To view a copy of this license, visit <http://creativecommons.org/licenses/by/4.0/>.

© The Author(s) 2023